

Magnetic Properties and Growth-Induced Anisotropy in Yttrium Thulium Iron Garnet Thin Films

Ethan R. Rosenberg,* Kai Litzius, Justin M. Shaw, Grant A. Riley, Geoffrey S. D. Beach, Hans T. Nembach, and Caroline A. Ross

Rare-earth iron garnets (REIG) have recently become the materials platform of choice for spintronic studies on ferrimagnetic insulators. However, thus far the materials studied have mainly been REIG with a single rare earth species such as thulium, yttrium, or terbium iron garnets. In this study, magnetometry, ferromagnetic resonance, and magneto-optical Kerr effect imaging is used to explore the continuous variation of magnetic properties as a function of composition for Y_xTm_{3-x} iron garnet ($Y_xTm_{3-x}IG$) thin films grown by pulsed laser deposition on gadolinium gallium garnet substrates. It is reported that the tunability of the magnetic anisotropy energy, with full control achieved over the type of anisotropy (from perpendicular, to isotropic, to an in-plane easy axis) on the same substrate. In addition, a nonmonotonic composition-dependent anisotropy term is reported, which is ascribed to growth-induced anisotropy similar to what is reported in garnet thin films grown by liquid-phase epitaxy. Ferromagnetic resonance shows linear variation of the damping and the g -factor across the composition range, consistent with prior theoretical work. Domain imaging reveals differences in reversal modes, remanent states, and domain sizes in Y_xTm_{3-x} iron-garnet thin films as a function of anisotropy.

1. Introduction

With the advent of vapor-phase growth methods for preparing thin epitaxial oxide films, including pulsed laser deposition

E. R. Rosenberg, K. Litzius, G. S. D. Beach, C. A. Ross
Department of Materials Science and Engineering
Massachusetts Institute of Technology
Cambridge, MA 02139, USA
E-mail: errosen@mit.edu

K. Litzius
Department of Modern Magnetic Systems
Max Planck Institute for Intelligent Systems
Stuttgart 70569, Germany

J. M. Shaw, G. A. Riley, H. T. Nembach
Quantum Electromagnetics Division
National Institute of Standards and Technology
Boulder, CO 80305, USA

H. T. Nembach
Department of Physics
University of Colorado
Boulder, CO 80309, USA

 The ORCID identification number(s) for the author(s) of this article can be found under <https://doi.org/10.1002/aelm.202100452>.

DOI: 10.1002/aelm.202100452

(PLD) and sputtering, thin films of rare earth (RE) iron garnet materials (REIG, formula unit $RE_3Fe_5O_{12}$) have been developed with desirable properties for spintronic applications, including thulium (TmIG), terbium, europium, samarium and other REIG films with perpendicular magnetic anisotropy (PMA). Spin-orbit torque switching,^[1,2] chiral spin textures,^[3–5] and a relativistic domain wall velocity approaching the magnon group velocity have been reported in Pt/TmIG and Pt/Bi:YIG heterostructures, making these materials promising candidates for memory or logic devices.^[4–7]

REIG materials are well-characterized, with studies having been performed from the 1950s to the present day. REIG materials have three magnetic sublattices, comprised of 3 RE^{3+} ions per formula unit (FU) on dodecahedral (c) sites, 2 Fe^{3+} /FU ions on octahedral (a) sites, and 3 Fe^{3+} /FU ions on tetrahedral (d) sites.^[8]

The strongest superexchange coupling is an antiferromagnetic interaction between the tetrahedral and octahedral iron. The dodecahedral moments are also coupled antiparallel to the tetrahedral iron, and hence the three sublattices form a collinear ferrimagnet, with the Fe^{3+} d ions opposing the combined moment of the RE^{3+} c and the Fe^{3+} a ions,^[8] though noncollinear ordering can occur at low temperatures by canting of the RE moments.^[9] Substitution of other cations has been explored extensively, with many cations exhibiting a site preference, for instance, Sc^{3+} on the a sites, Si on the d sites, and almost any RE element as well as yttrium (Y) on the c sites.^[10] Tuning the magnetic properties of REIG thin films, including the magnetization, anisotropy, coercivity, magnetostriction, compensation temperature and damping, has been investigated through control of the RE ion, the RE:Fe ratio, oxygen content, and substrate strain.^[11–13] In PLD or sputtered garnet films, PMA can be introduced due to magnetoelastic anisotropy,^[11,13–15] and has been controlled through strain engineering by varying the substrate epitaxial mismatch strain^[11,16] or the thermal mismatch strain^[17,18] and by altering the magnetostriction coefficients by fully substituting the RE species on the c -site.^[11,19,20] PMA of magnetoelastic origin has also been achieved in strained YIG^[21] and in Bi-substituted YIG,^[22] which exhibit lower damping than REIGs, and in garnets with multiple substitutions such as $(Dy,Ce)_3(Fe,Al)_5O_{12}$.^[23]

Table 1. Ratios of laser shots and nominal film compositions for Y:TmIG Films.

Nominal composition(Y_xTm_{3-x})Fe ₅ O ₁₂	Sample Recipe (Shot Ratio)	Shots YIG/cycle	Shots TmIG/cycle	Film Thickness, nm
TmIG	0:35 Y:TmIG	n/a	n/a	29
Y _{0.51} Tm _{2.49} IG	5:30 Y:TmIG	5	30	29
Y _{0.83} Tm _{2.17} IG	8:27 Y:TmIG	8	27	26
Y _{1.2} Tm _{1.8} IG	12:23 Y:TmIG	12	23	29
YIG	35:0 Y:TmIG	n/a	n/a	37

In contrast to these vapor-grown garnet films, the PMA in the liquid-phase-epitaxy-grown (LPE) REIG thin films of the late 1900s was attributed primarily to growth-induced anisotropy. This additional anisotropy energy was empirically shown to be a function of the difference in ionic radius between the c-site ions, and was believed to be caused by preferential occupation of inequivalent c sites by different species.^[24] The perpendicular anisotropy in PLD-grown Bi:YIG was attributed in part to growth-induced anisotropy.^[22] Also, iron vacancy ordering in Fe-deficient PLD-grown YIG was found to cause an additional uniaxial anisotropy.^[25] Other than these two studies, there have been scant reports of growth-induced anisotropy in vapor-deposited REIG films.^[22]

In this article, we describe the composition-dependent magnetic properties of yttrium-thulium iron garnet (YTmIG) thin films grown epitaxially on garnet substrates and demonstrate the presence of growth-induced perpendicular magnetic anisotropy. By varying the yttrium concentration over a limited range, we can tune the magnetic anisotropy energy and obtain a transition from perpendicular to isotropic to in-plane anisotropy. Magneto-optical Kerr effect (MOKE) microscopy is used to determine the equilibrium domain size and the reversal mode of YTmIG thin films with PMA. Broadband ferromagnetic resonance (FMR) measurements show an increase in the damping and a decrease in the g-factor with increasing Tm content, consistent with the Kittel model for bulk RE garnet crystals. These results demonstrate a method for continuously tuning a variety of REIG static and dynamic magnetic properties on a single substrate for spintronic applications.

2. Growth and Structural Characterization

For this study, Y_xTm_{3-x}IG (YTmIG) films ranging from 25 to 30 nm in thickness were grown by PLD on (111) gadolinium gallium garnet (Gd₃Ga₅O₁₂, GGG) substrates. YTmIG films were also grown on (111) substrates with composition Gd_{2.6}Ca_{0.4}Ga_{4.1}Mg_{0.25}Zr_{0.65}O₁₂ (substituted GGG or SGGG). The growth conditions (O₂ pressure, temperature, laser fluence) used were similar to those used in our previous work.^[4,5,11,26] described in the Experimental Section. In order to vary the composition *x*, YIG and TmIG targets were placed in the deposition chamber and the laser was fired alternately at each for a few shots at a time, keeping the total number of shots per cycle at 35 and the total number of shots per film at 10⁴. Thus, the total number of cycles was 285 for the co-deposited films. Film thicknesses were obtained by fitting X-ray reflectometry data. To obtain an estimate of the film composition, the growth rates for

YIG and TmIG films were measured for calibration. The YIG growth rate is 1.28 times higher than the TmIG growth rate, so the shot ratios were scaled by this factor to yield nominal compositions. A summary of the samples grown, their thicknesses, and their nominal compositions is provided in **Table 1**.

In order to characterize the structural properties of these films, high resolution X-ray diffraction (HRXRD) symmetric scans about the (444) direction were performed (**Figure 1a**). The high crystalline quality of the samples is evident from the Laue fringes present in each scan (also see the rocking curve analysis in Figure S4, Supporting Information). For the films with higher Y concentrations, the film peak was too close to the substrate peak to be fitted by a Gaussian function. Therefore, shear strain values were calculated by fitting both the substrate and film peaks with a commercially available dynamical diffraction software (Rigaku Globalfit). A model was constructed by considering the film to be an alloy between two hypothetical end-members whose (444) reflections were either to the left or to the right of all of the film peaks studied. Then, Vegard's law was used to calculate the lattice parameter of the films. By using the rhombohedral-to-hexagonal transformation described in our previous work^[11] and making the assumptions that the films are fully strained to match the substrate (i.e., the in-plane lattice parameters of the film and the substrate are equal) and that the unit cell side length is not significantly distorted by the shear strain, the unit cell corner angle (**Figure 1b**) for each film was calculated. The first assumption is well-justified by our previous work which showed that garnet films on GGG remain pseudomorphic (follow the substrate in-plane lattice parameter) up to thicknesses much greater than 30 nm.^[11] The second assumption is well-justified because it conserves unit cell volume to within 0.01%. The shear strain is then equal to $\pi/4 - \beta/2$. The shear strain values and unit cell angles are displayed in **Figure 1c**. Error bars were calculated but were excluded from the figure because they are smaller than the size of the displayed data points.

The lattice parameters of bulk TmIG and bulk YIG are 1.2324 and 1.2377 nm respectively (with a possible uncertainty of ± 0.001 nm determined from multiple reported measurements).^[8] The lattice parameters of the GGG and SGGG substrates are 1.2376 and 1.2480 nm respectively. It has been observed that the lattice parameters of c-site substituted garnets vary linearly between the two end-members.^[24] Therefore, YTmIG films grown on either substrate are expected to exhibit tensile in plane strain which decreases with increasing yttrium content. **Figure 1c** shows that as the composition changes from TmIG to YIG, the shear strain for films on GGG decreases from a tensile strain of 0.00153 to a compressive strain of 0.000715,

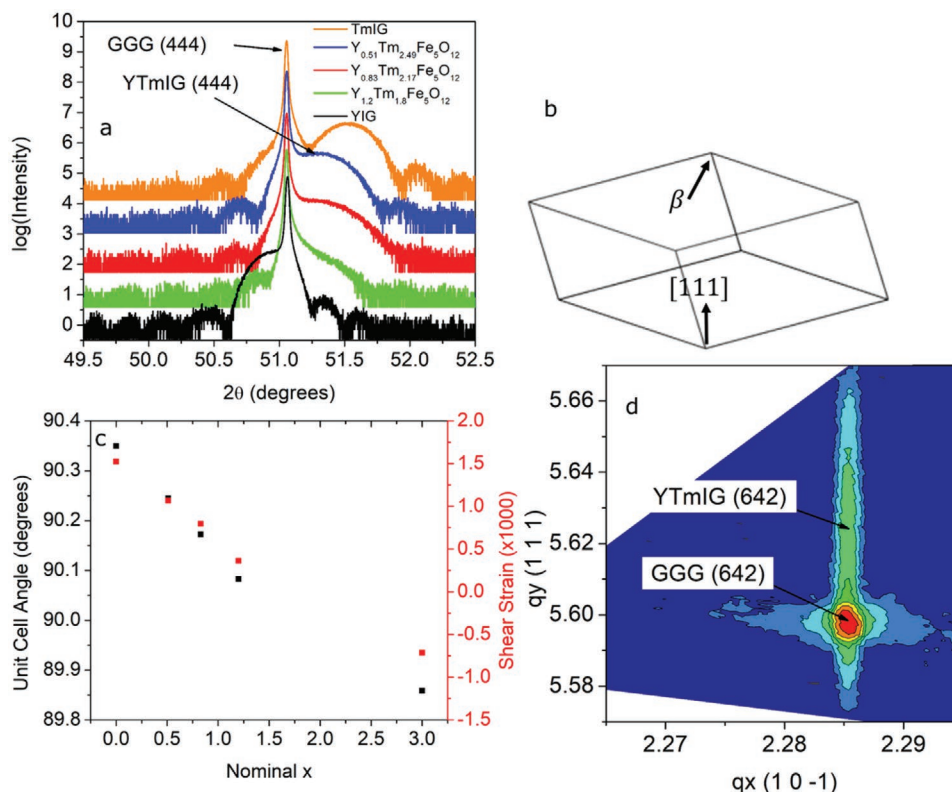


Figure 1. Structural Characterization of $Y_xTm_{3-x}IG$ thin films. a) HRXRD 2θ - ω spectra about the (444) reflection of five films of different composition. b) Schematic depicting the unit cell defining the corner angle β . c) Unit cell angle β (black squares) and shear strain in radians (red circles) of the $Y_xTm_{3-x}IG$ thin films. d) Reciprocal space map of the $Y_{0.83}Tm_{2.17}IG$ (642) reflection. The vertical alignment of the film and substrate peaks with a common value of qx is indicative of pseudomorphic growth.

following the predicted trend. Bulk YIG has an excellent lattice match with GGG, but the YIG film in our study is under in-plane compression. This is consistent with reports of larger-than-bulk lattice parameters in YIG, which are often attributed to iron vacancy formation due to non-ideal stoichiometry^[27–29] but have also been seen in stoichiometric YIG and are not fully understood.^[30] X-ray photoelectron spectroscopy (XPS) measurements of our pure YIG film, when compared to a stoichiometric bulk crystal (see the Supporting Information) show that the film is iron-rich with Y:Fe = 0.511.

For the $Y_{0.83}Tm_{2.17}IG$ and the $Y_{1.2}Tm_{1.8}IG$ films, a good fit to the Laue fringes of the high resolution XRD peaks was obtained using a multilayer model, i.e., relaxing the constraint that the lattice parameter is uniform through the thickness of the film (Figures S1 and S2, Supporting Information). The peaks were fitted with a combination of two layers of different lattice parameters. We attribute this behavior to a through-thickness out-of-plane strain gradient that leaves the film pseudomorphic. Strain gradients have been reported in YIG/GGG^[31] and do not preclude garnet films from being pseudomorphic^[32] – indeed, a reciprocal space map taken on the $Y_{0.83}Tm_{2.17}IG$ film confirmed that it was fully strained in-plane throughout its thickness (Figure 1d). Another possible source for the lattice parameter variation is cation segregation. Through-thickness composition gradients have been observed in ultrathin perovskite films grown under strain,^[33–35] explained

as a result of the accommodation of strain energy by the segregation of differently sized ions during growth. This mechanism may apply in YTmIG if Y^{3+} (the larger ion, Shannon radius 1.019 nm c.f. Tm^{3+} , 0.994 nm)^[36] is enriched near the substrate interface to reduce the in-plane tensile strain. However, XPS depth profile analyses on these two films (Figure S3, Supporting Information) did not find any significant gradient in the composition, implying that the gradient in the lattice parameter used to fit the XRD data results from a strain gradient. Regardless of the origin of the lattice parameter gradient, the calculated unit cell angles follow the trend expected from the composition, and the analysis yields the average shear strain through the thickness of the film.

3. VSM Characterization and Anisotropy Analysis

Vibrating sample magnetometer (VSM) measurements were performed, **Figure 2a,b**, to determine the effect of Y:Tm composition on the magnetic hysteresis loops of films on GGG. As the yttrium content increases, the out-of-plane loops become increasingly sheared and the in-plane saturation field decreases. Figure 2c shows the saturation magnetization M_s versus composition. The saturation magnetization increases with increasing yttrium content consistent with the higher M_s of YIG compared to TmIG. The large paramagnetic background

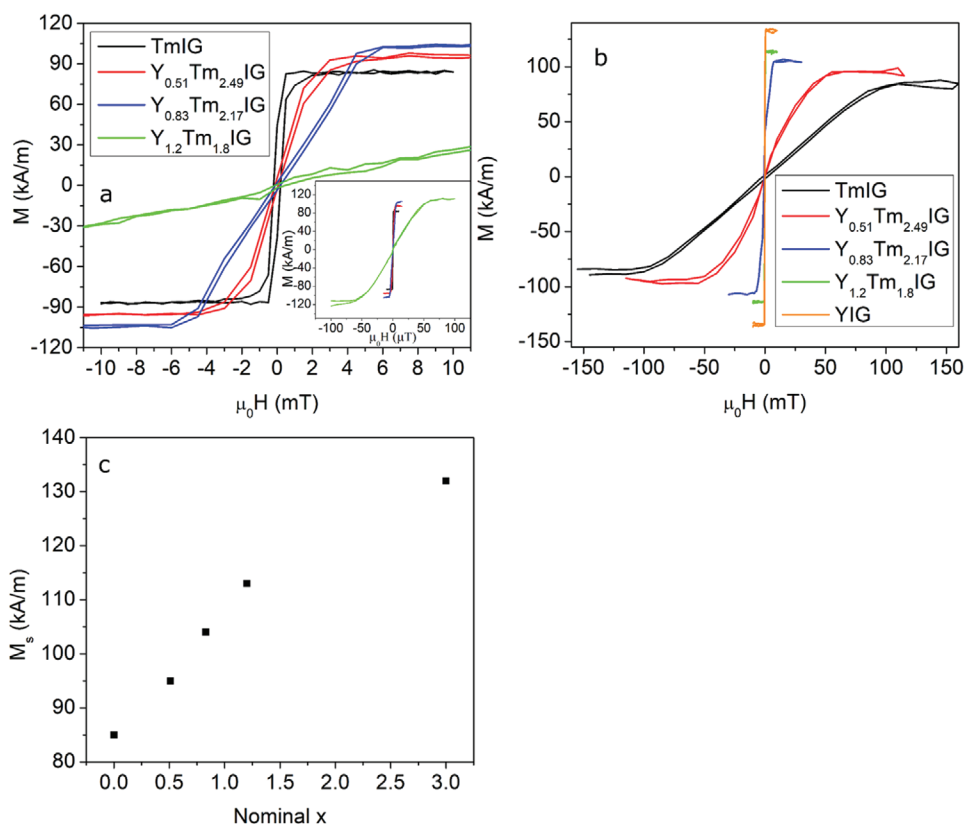


Figure 2. a) Out-of-plane and b) in-plane VSM hysteresis loops from the $Y_xTm_{3-x}IG/GGG$ thin films. To account for the difference in VSM sensitivity in the in-plane and out-of-plane geometries, the in-plane M_s was scaled to match the out-of-plane M_s for each film. The YIG out-of-plane hysteresis loop is omitted because its large out-of-plane saturation field impeded background subtraction. c) Saturation magnetization as a function of Y content in $Y_xTm_{3-x}IG/GGG$.

signal of the GGG substrate prevented background subtraction for the out-of-plane (hard axis) hysteresis loop of the YIG/GGG film. The saturation magnetization M_s of YIG was therefore measured from a YIG/SGGG sample that was grown simultaneously with the YIG/GGG. As shown in the Supporting Information, the films grown on GGG and SGGG have identical saturation magnetizations measured from the in-plane hysteresis loop. The anisotropy energy of all the films was also obtained from FMR measurements (see below).

The Y:Tm ratio has a profound impact on the magnetic anisotropy. TmIG/GGG exhibits PMA, similar to previous reports.^[14,16,37] Addition of Y reduces the anisotropy and $Y_{0.83}Tm_{2.17}IG/GGG$ is close to isotropic, with similar in-plane and out-of-plane loops. A further increase in Y content (as in $Y_{1.2}Tm_{1.8}IG$) gives rise to an in-plane magnetic anisotropy. To quantitatively extract the magnetic anisotropy energy (MAE) from VSM data, we measure the area enclosed by the $H > 0$ portions of the easy and hard axis loops, after eliminating any hysteresis by averaging the ascending and descending branches.^[38] The MAE is plotted in Figure 3a, varying from 4.6 kJ m⁻³ for TmIG/GGG (PMA) to ≈ 0 for $Y_{0.83}Tm_{2.17}IG/GGG$ and -3.1 kJ m⁻³ for $Y_{1.2}Tm_{1.8}IG/GGG$ (i.e., in-plane easy axis).

The MAE in the (111)-oriented epitaxial iron garnet films can be written as follows, with E_{IP} and E_{OP} the energy when the

magnetization is oriented in plane (IP) or out of plane (OP) respectively:

$$MAE = E_{OP} - E_{IP} = K_u + K_{shape} = -\frac{K_1}{12} + \frac{9}{4}\lambda_{111}c_{44}\left(\frac{\pi}{2} - \beta\right) + K_G - \left(\frac{\mu_0}{2}\right)M_s^2 \quad (1)$$

This expression includes the magnetocrystalline energy K_1 , the magnetoelastic energy which is a function of magnetostriction λ_{111} , shear strain $\frac{1}{2}\left(\frac{\pi}{2} - \beta\right)$ and shear modulus c_{44} , and the shape anisotropy $\mu_0 M_s^2/2$. The expression is modified from prior work^[11,14] by adding a uniaxial growth anisotropy K_G . K_u , which is plotted in Figure 3b, represents the sum of anisotropies that compete with the shape anisotropy to yield PMA when $|K_u| > |K_{shape}|$. The sign convention gives a positive MAE for films with PMA. The magnetocrystalline contribution is small for REIGs at room temperature.^[8]

The substitution of Y for Tm affects the anisotropy terms in Equation (1). First, the M_s of YIG is higher than that of TmIG so substituting Y will increase the shape anisotropy and lower PMA. Second, increasing Y raises the lattice parameter which lowers the tensile shear strain, and Y also lowers the magnetostriction. Bulk YIG has a lower than TmIG, -2.73×10^{-6} for YIG and -5.2×10^{-6} for TmIG.^[8] The lower strain and

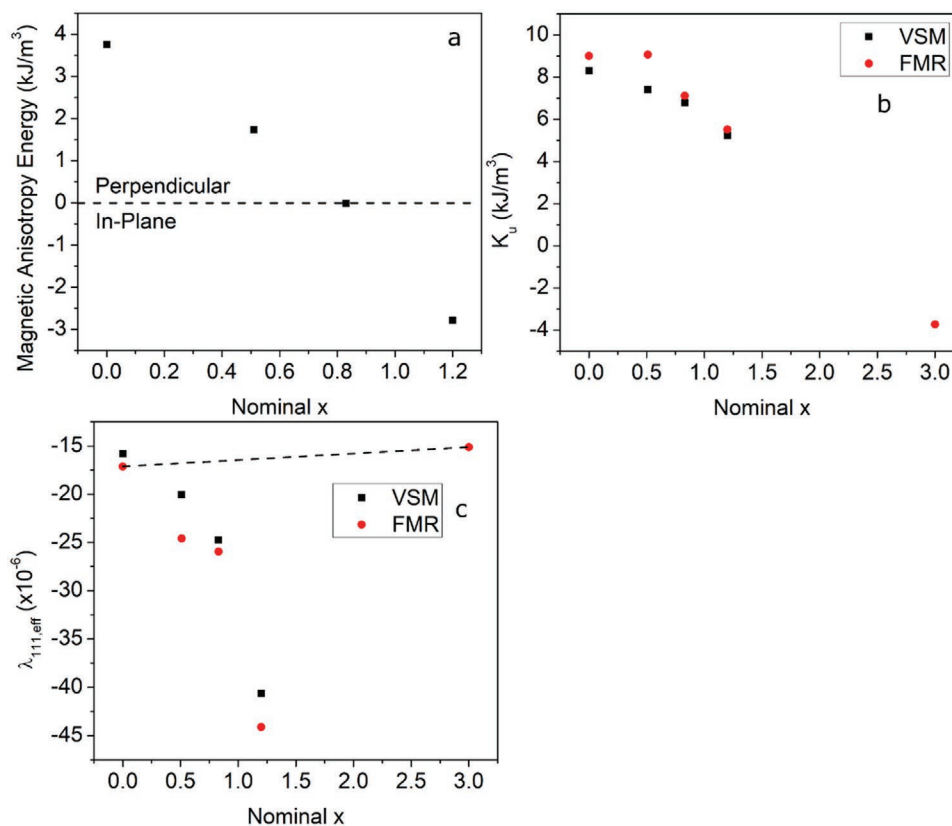


Figure 3. Extracted anisotropy and magnetostriction data. a) Total magnetic anisotropy (including shape anisotropy) calculated by integrating the area between the out-of-plane and in-plane hysteresis loops in Figure 2. b) Uniaxial anisotropy (not including shape anisotropy), calculated from both VSM and FMR data. The $x = 3$ point (YIG) was derived from FMR not VSM. c) Calculated effective magnetostriction $\lambda_{111,eff}$ for the $Y_xTm_{3-x}IG$ films derived from Equation (1) and the FMR K_u values. The dotted line is the interpolated anisotropy from the rule of mixtures.

magnetostriction resulting from Y substitution therefore reduces the magnetoelastic contribution to PMA.

In Equation (1), the shape anisotropy term is obtained from M_s , the unit cell angle β is determined from the XRD analysis, and the shear modulus c_{44} is taken as that of YIG,^[8] 766 GPa. Reported c_{44} values for YIG, EuIG, and GdIG are within 3% of each other, indicating that c_{44} for iron garnets is weakly dependent on the rare-earth species.^[8] The bulk $K_1 = -610 \text{ J m}^{-3}$ for YIG and -580 J m^{-3} for TmIG^[8] provides a negligible contribution to the total anisotropy of the samples. Taking these bulk values as a reference, $K_1/12$ is $\approx 50 \text{ J m}^{-3}$, two orders of magnitude lower than the observed shape and uniaxial anisotropies. Without considering K_C , we derive effective values of $\lambda_{111,eff}$ as shown in Figure 3c. Two striking features of these data are immediately evident. First, the value of $\lambda_{111,eff}$ for both end members TmIG and YIG (based on the anisotropy energy determined by FMR) are larger than the bulk values. Second, there is an increase (rather than a decrease) of $\lambda_{111,eff}$ with Y content for the films containing both Y and Tm. For bulk garnets,^[8] the magnetostriction follows the rule of mixtures, i.e., a linear interpolation between the two end members, but in our films the intermediate compositions have an effective magnetostriction far greater than those of YIG and TmIG.

These observations suggest that there is an additional source of anisotropy beyond the magnetocrystalline, shape, and magnetoelastic anisotropy terms, identified by the term K_C in

Equation (1). One possible origin of the additional anisotropy is growth-induced ordering of the dodecahedral-site cations, similar to what has been observed in thicker films of mixed-composition garnets grown by liquid phase epitaxy (LPE).^[24] The mechanism for this form of anisotropy is the preferential incorporation of rare-earth cations into inequivalent dodecahedral sites in the crystal lattice on the basis of their size. This broken symmetry yields an additional uniaxial anisotropy term in (111)-oriented films.^[24] Growth-induced anisotropy is proportional to $x(3-x)^2$ where x is the yttrium content ($0 \leq x \leq 3$), i.e., the growth-induced anisotropy would be maximized for a Y:Tm = 1:1 composition.^[24] On the basis that $K_C = 0$ for the end-members TmIG and YIG, and that λ_{111} is given by a linear interpolation between the magnetostriction of the endmembers, we determine K_C for the intermediate compositions as shown in Table 2. For this calculation, the nominal compositions from Table 1 were used. Note that, for consistency, FMR data was used to derive K_u and the interpolated λ_{111} because the anisotropy field of YIG was not measurable by VSM.

Growth-induced anisotropy has been studied mainly in LPE-grown garnets,^[24,39–41] but recently its existence was inferred in PLD-grown Bi:YIG thin films^[22] through an analysis similar to this work. In LPE growth, YTmIG films would not be expected to exhibit growth-induced anisotropy because the ionic size difference of 2.5 pm between Y^{3+} and Tm^{3+} ions is smaller than the size difference of 5 pm required for the onset of growth-induced

Table 2. Interpolated Magnetostriction and Calculated K_C for YTmIG/GGG Films.

Sample	Interpolated λ_{111} , $\times 10^{-6}$ (FMR-derived)	Growth-Induced Anisotropy Energy K_C [J m $^{-3}$]
TmIG	-17.12 ± 0.04	0
Y $_{0.51}$ Tm $_{2.49}$ IG	-16.78 ± 0.03	2890 ± 20
Y $_{0.83}$ Tm $_{2.17}$ IG	-16.56 ± 0.04	2580 ± 10
Y $_{1.2}$ Tm $_{1.8}$ IG	-16.32 ± 0.08	3470 ± 10
YIG	-15.11 ± 0.04	0

anisotropy.^[24] This could imply that growth-induced anisotropy appears more readily under the non-equilibrium conditions that prevail during in PLD growth.

However, growth-induced anisotropy from dodecahedral ordering alone cannot explain the large excess magnetostriction in the TmIG and YIG films compared to bulk. EuIG films were also reported to have a magnetostriction exceeding the bulk values.^[11] A significant difference in c_{44} values for PLD-grown garnets appears unlikely, because a study on LPE-grown Bi:YIG showed c_{44} very close to bulk.^[42] One possibility is the existence of growth-induced anisotropy from cation ordering on the iron sublattice. Previous work on iron-deficient YIG has shown that vacancies preferentially form on the octahedral sublattice during PLD growth, giving rise to an additional growth induced anisotropy.^[25] Our YIG is Fe-rich (see Section S4 in the Supporting Information). Therefore, there may be two forms of growth-induced anisotropy operating in the YTmIG films: one induced by ordering of Y and Tm on the dodecahedral sites (observed unequivocally in the non-monotonic variation of $\lambda_{111, \text{eff}}$) and one induced by ordering of antisites, vacancies or other point defects resulting from non-ideal stoichiometry (observed in the higher-than-bulk magnetostrictions of the end-member films). However, additional work simultaneously varying the dodecahedral and the octahedral/tetrahedral site occupancies would be necessary to confirm this hypothesis.

4. FMR Characterization

The dynamic magnetic properties of the YTmIG films were studied with broadband perpendicular FMR spectroscopy based on the vector network analyzer (VNA) technique.^[43–46] A static out-of-plane magnetic field up to $\mu_0 H = 2.2$ T was swept while a fixed microwave field with a frequency as high as 40 GHz was applied via a coplanar waveguide with a 100 μm wide center conductor. For certain positions on the films, multiple closely-spaced resonances were observed (see Section S5 in the Supporting Information), which we ascribe to regions with slightly different anisotropy values. As we will show later, such regions were observed via MOKE microscopy. For all samples except for the pure YIG film, regions with a single resonance could be found; fits to the single-peak data were used to calculate the materials parameters as described below. Broad resonances in the spectra originate from the GGG substrates (Section S6, Supporting Information).

The complex susceptibilities of the films were extracted from the complex transmission parameters S_{21} via the relationships

derived in reference 44 (Figure 4a). Then, using the procedure described in reference 43, the effective magnetization M_{eff} and the Landé g-factor were extracted using the Kittel equation for the perpendicular geometry:

$$H_{\text{res}} = \frac{2\pi f}{|\gamma| \mu_0} + M_{\text{eff}} \quad (2)$$

In this expression, H_{res} is the resonance field, f is the excitation frequency, and γ is the gyromagnetic ratio ($g\mu_B$)/ \hbar where μ_B is the Bohr magneton and \hbar is the reduced Planck constant. In order to confirm the agreement between the VSM measurements and the FMR results, K_u is extracted from M_{eff} from the equation^[37,47]

$$M_{\text{eff}} = M_s - \frac{2K_u}{\mu_0 M_s} \quad (3)$$

The results of these calculations are presented in Figure 3b, where we can see good agreement between the VSM-derived and FMR-derived anisotropy values. This also provides an independent confirmation of the existence of the excess anisotropy discussed in the previous section.

The damping α was extracted using the expression:

$$\Delta H = \frac{4\pi\alpha f}{|\gamma| \mu_0} + \Delta H_0 \quad (4)$$

where ΔH is the experimentally observed linewidth determined from fitting the S_{21} data with the complex susceptibility and ΔH_0 is the inhomogeneous broadening linewidth.^[48] Exemplary fits for ΔH and H_{res} are displayed in Figure 4b.

The extracted g-factor values (Figure 4c) show a monotonic increase from 1.5744 ± 0.0007 for TmIG to 1.7701 ± 0.0004 for $x = 1.2$. These values are significantly lower than the value of 2 expected for a free electron. In order to explain the values and trends in g-factor with x , we can apply a simple two-sublattice model based on the Landau-Lifshitz (LL) equation which was originally derived by Kittel^[49] to describe g-factors in rare-earth-substituted YIG. The central assumption in this model are that the damping on the rare-earth sublattice is much larger than the damping on the iron sublattice; upon making this assumption and solving the secular equation for the coupled LL equations for the rare earth and the net iron moments we obtain the simple relationship

$$g_{\text{eff}} = \frac{g_A (M_A + M_B)}{M_A} = g_A \left(1 - \frac{|M_B|}{|M_A|} \right) \quad (5)$$

where M_A and M_B are the saturation moments of the resultant iron and the rare-earth sublattices, respectively (note that in this model M_A and M_B have opposite signs). It is unknown how the M_s is apportioned between the iron and rare earth sublattices. Following Kittel, we make the additional assumption that M_A is identically equal to the M_s of YIG and that $M_A + M_B$ is identically equal to the M_s of a particular YTmIG sample:

$$g_{\text{eff}} = g_{\text{YIG}} \frac{M_s(\text{YTmIG})}{M_s(\text{YIG})} \quad (6)$$

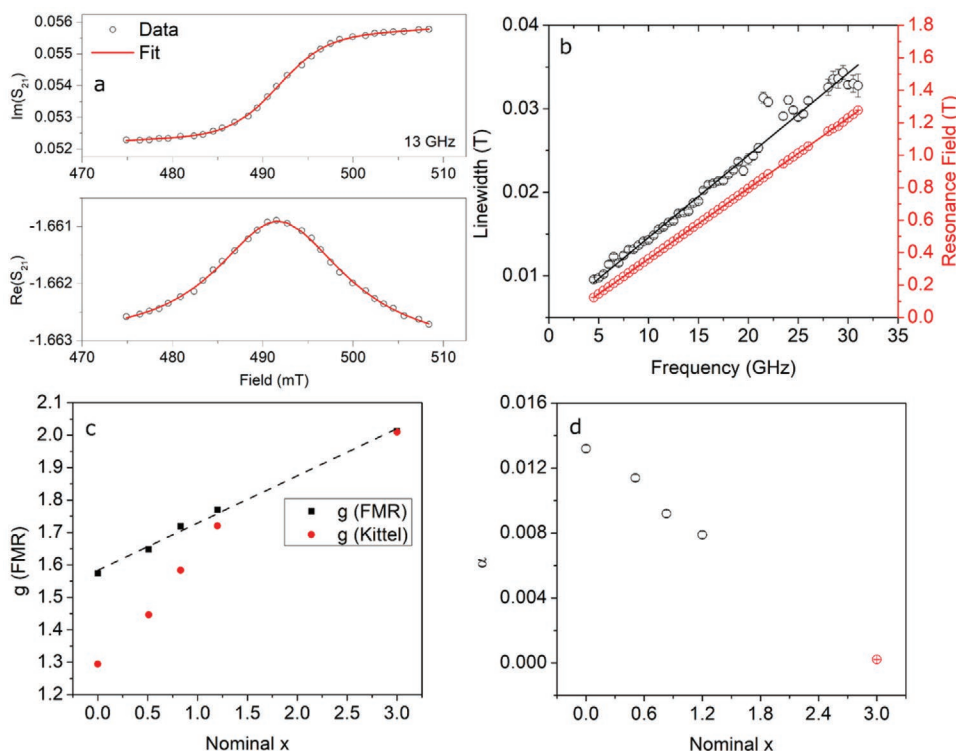


Figure 4. a) Representative fits of FMR spectra from the $Y_{0.51}Tm_{2.49}IG$ thin film. b) Representative fits of ΔH versus frequency (black) and H_0 versus frequency (red) from the $Y_{0.51}Tm_{2.49}IG$ thin film. c) g -factor versus x . The red points are calculated by the Kittel model, and the dotted line is the linear fit to the data. d) Damping versus composition, x . The red point is from a previously reported YIG film.^[50]

Using the measured values for the M_s of YIG and YTMIG, we obtain the theoretical estimate of g_{eff} which is plotted in Figure 4c. Both the model and the experimental values converge for the YIG/GGG film, which possesses a bulk-like g factor of 2.0132 ± 0.0003 . However, while the model agrees with the experiment in that both show a linear dependence of g_{eff} on the Y concentration, the slope of the model curve is steeper than that of the experiment. This is likely due to the sublattice contributions to M_s in TmIG being different than in YIG – a possibility discussed in ref. [49]. To investigate this possibility, we can further manipulate the Kittel model by relaxing the assumption that $M_A = M_{\text{YIG}}$ and instead allowing M_A to vary. To obtain a linear dependence, we assume instead that $|M_B|/M_A$ varies linearly with x and obtain:

$$g = g_A \left(1 - 3 \left(\frac{|M_B|}{M_A} \right)_0 \right) + g_A \left(\frac{|M_B|}{M_A} \right) x \quad (7)$$

Here, $(|M_B|/M_A)_0$ is the magnetization ratio when $x = 0$. A linear fit of our data to this expression yields the empirical expression:

$$g = (1.584 \pm 0.009) + (0.145 \pm 0.006)x \quad (8)$$

By matching slopes and using our experimentally measured value for g_A (the g -factor measured for $x = 3$), we calculate that $(|M_B|/M_A)_0 = 0.0720 \pm 0.0006$. To check for consistency,

we can calculate the new predicted y -intercept of the g -factor using this value; we obtain 1.578 ± 0.002 , which is within the error bar for our fit. Therefore, we can conclude that our assumption is correct: $|M_B|/M_A$ varies linearly with x , even though M_A is not a constant equal to M_{YIG} . Interestingly, our results are at odds with a previous report that M_A stays constant in $Y_{2.4-x}Tm_xBi_{0.6}Fe_{5-y}Ga_yO_{12}$ (for constant y).^[51] Sum rule analysis via X-ray absorption spectrometry/X-ray magnetic circular dichroism (XAS/XMCD) may help shed light on this discrepancy.

The damping values extracted from the FMR data are displayed in Figure 4d. Due to the multiple resonances mentioned earlier, a value for g was obtained for YIG but α could not be extracted from the data. Therefore, the red data point in Figure 4d is from YIG grown previously by our group using a similar PLD growth process.^[50] The damping values show a monotonic linear decrease from $(1.32 \pm 0.02) \times 10^{-2}$ for TmIG to the previously reported YIG value of $(2.2 \pm 0.2) \times 10^{-4}$. This is expected because rare-earth ions such as Tm^{3+} are known to relax rapidly compared to Fe ions.^[49] The TmIG value of α is comparable to previously reported values.^[52] This is in good agreement with Kittel's microscopic model of the linewidth in RE-substituted YIG^[53] and previous experimental work in Sm-substituted YIG.^[54] The linear decrease of damping with Y content suggests that low-damping YTMIG films with PMA can be grown by leveraging growth-induced and strain-induced anisotropy.

5. MOKE Analysis and Domain Characterization

As we have seen, the easy axis loops for the TmIG, $Y_{0.51}Tm_{2.49}IG$ and $Y_{0.83}Tm_{2.17}IG$ samples display increasing amounts of shear as the Y content increases. This is indicative of domain formation in PMA thin films. With decreasing uniaxial anisotropy, thin films with PMA cannot support a uniform out-of-plane magnetization at remanence and instead form stripe domains to reduce magnetostatic energy.^[55–57] Our recent work on TmIG using scanning transmission X-ray microscopy^[58] showed labyrinthine arrays of stripe domains. According to the seminal work on stripe domains by Kooy and Enz,^[57] the loop shearing and the saturation field will increase as M_s increases and K_u decreases.

Polar MOKE microscopy was used to image the domain morphologies of the TmIG and the $Y_{0.51}Tm_{2.49}IG$ films. In order to maximize contrast, an LED light source with a wavelength of 457 nm was used. Before imaging, an out of-plane AC demagnetization process with an exponentially decaying oscillating magnetic field was performed to promote a low-energy multidomain state. An image taken at saturation was subtracted to reduce nonmagnetic contrast. Representative images are displayed in Figure 5. In order to quantify the domain spacing, 2D fast Fourier transforms (2D FFT) were performed on the MOKE images and radial average intensities were extracted (Figure 5c). Gaussian peaks were fitted to these radial intensity distributions to determine the

average stripe spacing. In order to account for the effect of nonuniformity in the PLD growth, images were taken at multiple points on the samples and the resulting stripe spacings were averaged. As expected from the Kooy-Enz model, as more yttrium is added to the film, causing M_s to increase and K_u to decrease, the equilibrium stripe spacing decreases. The average equilibrium stripe spacing is $15 \mu\text{m} \pm 6 \mu\text{m}$ for TmIG and is $4 \mu\text{m} \pm 3 \mu\text{m}$ for $Y_{0.51}Tm_{2.49}IG$. Here, the reported error bars are the sample standard deviations of the extracted domain sizes for these two films. The spread in domain sizes across the films indicates some inhomogeneity in magnetic properties (e.g., uniaxial anisotropy and saturation magnetization) which likely explains the multiple resonances observed in FMR. From these domain size values, we can apply the model of Kaplan and Gehring^[59] in order to extract the domain wall energies of these films. This analytical model, which is a limiting case of the more general Kooy-Enz model^[57] for the situation where the film thickness is much less than the domain period, can be summarized in the equation:

$$D_s = t \exp\left(\frac{\pi b}{2} + 1\right) \exp\left(\frac{\pi \sigma_w}{2K_d t}\right) \quad (9)$$

Here, D_s is the stripe domain width, t is the film thickness, b is a model-dependent constant approximately equal to -0.666 , σ_w is the domain wall energy, and K_d is the dipolar energy constant $\mu_0 M_s^2 / 2$. From this, we can calculate the domain wall energies of TmIG and $Y_{0.51}Tm_{2.49}IG$ displayed in Table 3. These values are well in-line with reported bulk domain wall energies in rare-earth garnets, which are generally between 0.2×10^{-3} and $1 \times 10^{-3} \text{ J m}^{-2}$.^[8]

The TmIG and $Y_{0.51}Tm_{2.49}IG$ films are well above the thickness at which a crossover from Néel to Bloch walls have been observed in TmIG.^[5] By assuming that the walls are 180° Bloch walls we are able to estimate the exchange stiffness in these films as $A = \frac{\sigma_w^2}{16K_u}$. These estimates are also presented in Table 3 (the FMR-derived values for K_u were used). The TmIG film has a slightly lower exchange stiffness than the YTmIG film. Literature values for the exchange stiffness constants of undiluted garnets (i.e., garnets with no diamagnetic substitution on the iron sublattice) are rare. However, the reported value for YIG is lower than the reported value for the undiluted rare-earth garnet $Tb_{2.5}Er_{0.5}Fe_5O_{12}$,^[8] implying that the addition of Y to rare-earth garnets changes the exchange stiffness.

MOKE microscope hysteresis loops were collected to determine the reversal mechanism under DC fields for TmIG (Figure 6a) and the $Y_{0.51}Tm_{2.49}IG$ (Figure 6b) after saturation at ± 50 mT. For TmIG, low-field domain nucleation occurred at defects such as surface scratches in the substrate and domain growth proceeded outward from these defects. This process of nucleation on defects is repeatable, with reverse domains appearing at similar locations and applied fields for both the forward and reverse branches. Some regions of the film bounded by surface scratches switched within one field increment without forming domains. Also, the film has a non-zero remanence, as large regions remain un-switched at zero applied field. The surface scratches are present in the substrate prior to deposition, and the film grown at those locations is likely to

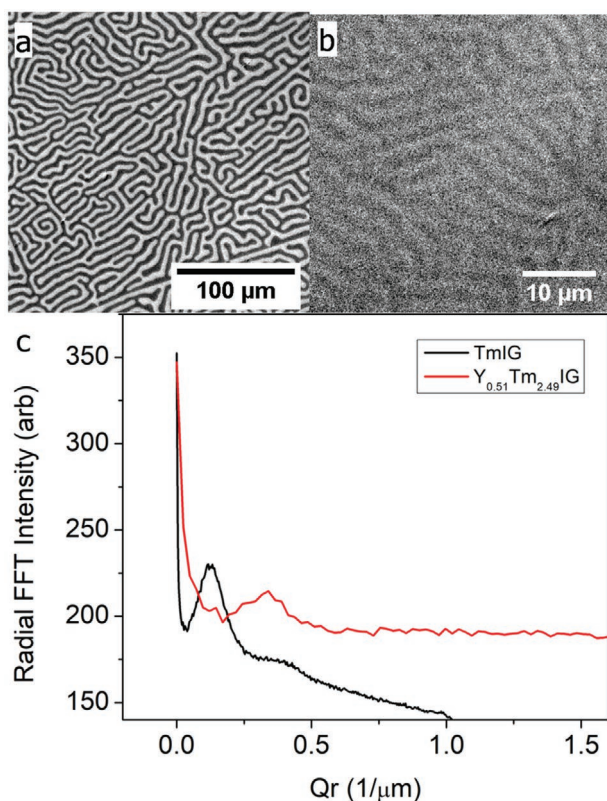


Figure 5. a,b) AC-demagnetized domain structure of TmIG (a) and $Y_{0.51}Tm_{2.49}IG$ (b). Note the different scale bars in each image. c) Radially averaged FFT spectra of the images in (a,b).

Table 3. Calculated Domain Wall Energy and Exchange Stiffness for TmIG and $Y_{0.51}Tm_{2.49}IG$.

Material	Domain Wall Energy [10^{-3} J m $^{-2}$]	Exchange Stiffness [10^{-12} J m $^{-1}$]
TmIG	0.527 ± 0.002	2.09 ± 0.002
$Y_{0.51}Tm_{2.49}IG$	0.535 ± 0.002	2.42 ± 0.002

have a different thickness, strain state and anisotropy from the film on smooth regions, providing a barrier for domain propagation and/or a site for nucleation.

For $Y_{0.51}Tm_{2.49}IG$, magnetic reversal occurs in a more continuous manner, with labyrinthine stripe domains occupying the full area as the field approaches zero. Near zero applied field, domain expansion occurs in a similar manner to that described in the Kooy-Enz model,^[57] with the majority domains expanding and the minority domains staying the same width but becoming more sparse. The surface scratches in the film perturb the domain structure, with reverse domains tending to nucleate parallel to the scratches before expanding away from

the scratches. However, domain nucleation is less clearly defect-mediated than for the TmIG film. The locations at which the domains parallel to the scratches branch into the regions adjacent to the scratches are different for the forward and reverse branches, and the reversal process is more homogeneous. The film has zero remanence at zero applied field corresponding to the presence of labyrinthine stripe domains.

The $Y_{0.83}Tm_{2.17}IG$ sample has a magnetic anisotropy energy about two orders of magnitude lower than that of the other samples, and was expected to have a continuously varying magnetization texture and/or weak stripe domains rather than the strong stripe domains seen in the $Y_{0.51}Tm_{2.49}IG$ sample.^[56,60] However, it exhibited no contrast in the MOKE microscope which may indicate a predominantly in plane or uniform magnetization.

6. Conclusion

In this study, a systematic exploration of PLD-grown $Y_xTm_{3-x}IG$ films was carried out across the range of substitution $x = 0$

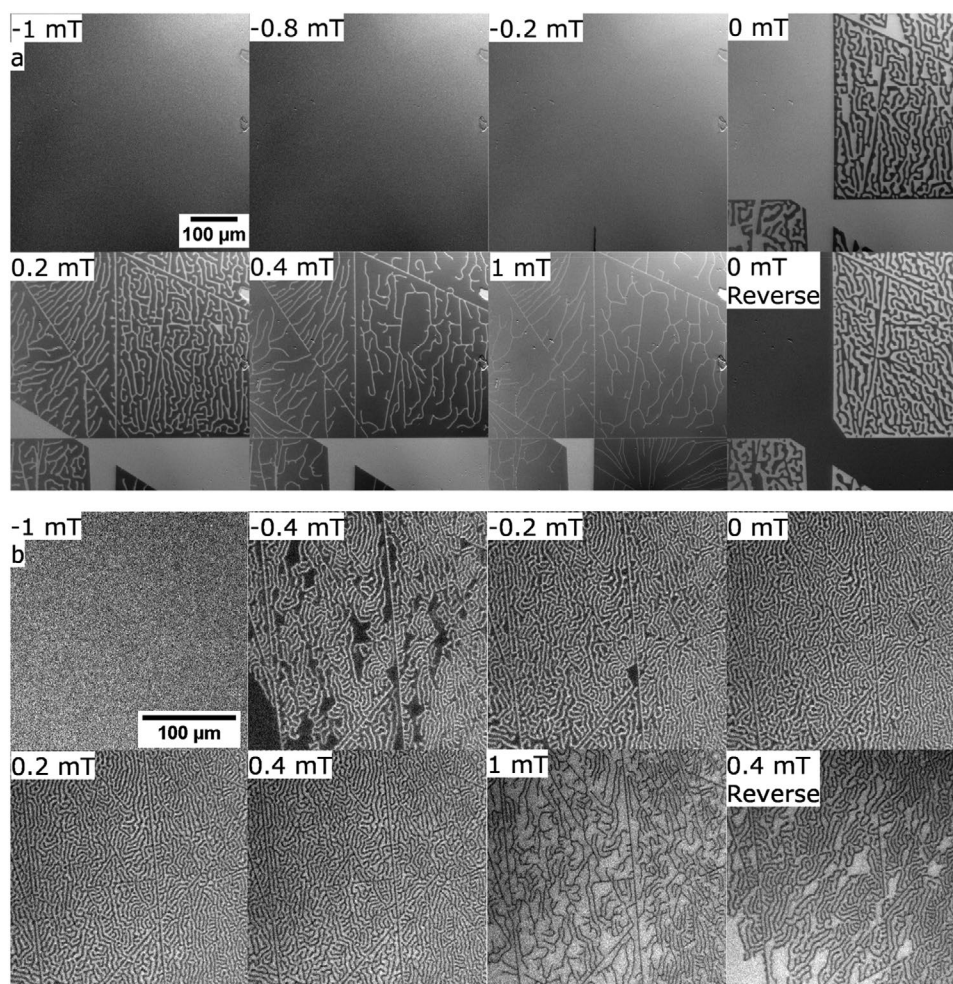


Figure 6. MOKE hysteresis loops of a) TmIG and b) $Y_{0.51}Fe_{2.49}IG$ demonstrating the difference in reversal mechanism for these two films. In each panel, one picture from the “reverse” branch of the hysteresis loops is shown to whether domains occur in the same locations in the ascending and descending branches. The “reverse” images were saturated at +50 mT and the others were saturated at –50 mT.

to 3. All the films are epitaxially matched to GGG and SGGG substrates with good crystalline quality. Films on GGG with $x = 0.83$ and 1.2 exhibit a through-thickness lattice parameter gradient which is attributed to a variation in strain rather than composition, and the films remain pseudomorphic to the substrate. Y-substitution has dramatic effects on the anisotropy of YTmIG thin films on GGG, with as little as $x = 0.8$ causing a reorientation from PMA to an in-plane easy axis. Films containing both Y and Tm exhibit a growth-induced anisotropy which varies non-monotonically with Y content. The observation is among the first reports of a growth-induced anisotropy in PLD-grown garnet films and it occurs with a cation pair, Y:Tm, which is not expected to show this form of anisotropy based on the small difference in their ionic radii. The domain morphologies and DC switching behavior of the TmIG and the $Y_{0.51}Tm_{2.49}IG$ film differed. TmIG has a larger equilibrium domain size than $Y_{0.51}Fe_{2.49}IG$, and it reverses by the movement of domain walls across large (10s μm) regions of the film. In contrast, $Y_{0.51}Fe_{2.49}IG$ exhibits zero remanence (also visible in its sheared hysteresis loop) and reverses through stripe domain growth similar to the classical Kooy-Enz model. FMR measurements showed that the g-factor varied with yttrium content, and the variation was compared with a simple model for RE-substituted YIG films. Damping was also found to vary linearly with Y content, in agreement with previously reported data on LPE-grown films. Through the range of growth-induced and magnetoelastic anisotropy, domain structure, damping, and g-factor on a single substrate, Y-substitution provides an important control parameter for designing PLD-grown garnet thin films for spintronic device applications.

7. Experimental Section

Thin Film Growth: All films were grown via pulsed laser deposition with a laser pulse energy of 300 mJ, a laser repetition rate of 10 Hz, a substrate-target distance of 8 cm, a substrate heater temperature of 900 °C with the substrate surface ≈ 150 °C lower, and an O_2 pressure of 150 mTorr. The number of shots per deposition was kept at 10000 for each film, and the number of shots per cycle was kept at 35 for the codeposited films. Commercially available YIG and TmIG targets and (S) GGG substrates from MTI Corp. were used.

Thin Film Characterization: 2θ - ω scans and reciprocal space maps were carried out using a Bruker D8 Discover diffractometer. The average lattice parameters of the films were extracted by fitting the 2θ - ω scans using the Rigaku Globalfit software (described in main text). In- and out-of-plane VSM hysteresis loops were collected in a DMS 880A VSM. MOKE microscope images were collected with a custom-built MOKE microscope system. In order to maximize MOKE contrast, a blue LED light source (wavelength = 457 nm) was used.

Certain commercial equipment, instruments, or materials are identified in this paper to foster understanding. Such identification does not imply recommendation or endorsement by the National Institute of Standards and Technology, nor does it imply that the materials or equipment identified are necessarily the best available for the purpose.

Supporting Information

Supporting Information is available from the Wiley Online Library or from the author.

Acknowledgements

The authors gratefully acknowledge support from NSF DMR 1911792, DARPA, and SMART, an nCORE Center of the SRC. MRSEC shared facilities under DMR 1419807 were used.

Conflict of Interest

The authors declare no conflict of interest.

Data Availability Statement

Research data are not shared.

Keywords

garnets, magnetic materials, pulsed laser deposition, spintronics, thin films

Received: May 10, 2021

Revised: June 22, 2021

Published online:

- [1] C. O. Avci, A. Quindeau, C.-F. Pai, M. Mann, L. Caretta, A. S. Tang, M. C. Onbasli, C. A. Ross, G. S. D. Beach, *Nat. Mater.* **2017**, *16*, 309.
- [2] C. O. Avci, E. Rosenberg, M. Baumgartner, L. Beran, A. Quindeau, P. Gambardella, C. A. Ross, G. S. D. Beach, *Appl. Phys. Lett.* **2017**, *111*, 072406.
- [3] S. Ding, A. Ross, R. Lebrun, S. Becker, K. Lee, I. Boventer, S. Das, Y. Kurokawa, S. Gupta, J. Yang, G. Jakob, M. Kläui, *Phys. Rev. B* **2019**, *100*, 100406.
- [4] C. O. Avci, E. Rosenberg, L. Caretta, F. Büttner, M. Mann, C. Marcus, D. Bono, C. A. Ross, G. S. D. Beach, *Nat. Nanotechnol.* **2019**, *14*, 561.
- [5] L. Caretta, E. Rosenberg, F. Büttner, T. Fakhrlul, P. Gargiani, M. Valvidares, Z. Chen, P. Reddy, D. A. Muller, C. A. Ross, G. S. D. Beach, *Nat. Commun.* **2020**, *11*, 1090.
- [6] S. Vélez, J. Schaab, M. S. Wörnle, M. Müller, E. Gradauskaite, P. Welter, C. Gutschell, C. Nistor, C. L. Degen, M. Trassin, M. Fiebig, P. Gambardella, *Nat. Commun.* **2019**, *10*, 4750.
- [7] L. Caretta, S. H. Oh, T. Fakhrlul, D. K. Lee, B. H. Lee, S. K. Kim, C. A. Ross, K. J. Lee, G. S. D. Beach, *Science* **2020**, *370*, 1438.
- [8] K.-H. Hellwege, A. M. Hellwege, *Landolt-Börnstein – Group III Crystal and Solid State Physics Vol 12a*, Springer-Verlag, Berlin/Heidelberg **1978**.
- [9] M. Lahoubi, M. Guillot, A. Marchand, F. Tcheou, E. Roudault, *IEEE Trans. Magn.* **1984**, *20*, 1518.
- [10] S. Geller, *J. Appl. Phys.* **1966**, *37*, 1408.
- [11] E. R. Rosenberg, L. Beran, C. O. Avci, C. Zeledon, B. Song, C. Gonzalez-Fuentes, J. Mendil, P. Gambardella, M. Veis, C. Garcia, G. S. D. Beach, C. A. Ross, *Phys. Rev. Mater.* **2018**, *2*, 094405.
- [12] C. N. Wu, C. C. Tseng, K. Y. Lin, C. K. Cheng, S. L. Yeh, Y. T. Fanchiang, M. Hong, J. Kwo, *AIP Adv.* **2018**, *8*, 055904.
- [13] M. Kubota, K. Shibuya, Y. Tokunaga, F. Kagawa, A. Tsukazaki, Y. Tokura, M. Kawasaki, *J. Magn. Magn. Mater.* **2013**, *339*, 63.
- [14] A. Quindeau, C. O. Avci, W. Liu, C. Sun, M. Mann, A. S. Tang, M. C. Onbasli, D. Bono, P. M. Voyles, Y. Xu, J. Robinson, G. S. D. Beach, C. A. Ross, *Adv. Electron. Mater.* **2016**, *3*, 1600376.

- [15] M. Kubota, A. Tsukazaki, F. Kagawa, K. Shibuya, Y. Tokunaga, M. Kawasaki, Y. Tokura, *Appl. Phys. Express* **2012**, 5, 103002.
- [16] G. Vilela, H. Chi, G. Stephen, C. Settens, P. Zhou, Y. Ou, D. Suri, D. Heiman, J. S. Moodera, *J. Appl. Phys.* **2020**, 127, 115302.
- [17] J. J. Bauer, E. R. Rosenberg, S. Kundu, K. A. Mkhoyan, P. Quarterman, A. J. Grutter, B. J. Kirby, J. A. Borchers, C. A. Ross, *Adv. Electron. Mater.* **2020**, 6, 1900820.
- [18] J. J. Bauer, E. R. Rosenberg, C. A. Ross, *Appl. Phys. Lett.* **2019**, 114, 052403.
- [19] V. H. Ortiz, M. Aldosary, J. Li, Y. Xu, M. I. Lohmann, P. Sellappan, Y. Kodera, J. E. Garay, J. Shi, *APL Mater.* **2018**, 6, 121113.
- [20] S. Mokarian Zanjani, M. C. Onbaşlı, *J. Magn. Magn. Mater.* **2020**, 499, 166108.
- [21] G. Li, H. Bai, J. Su, Z. Z. Zhu, Y. Zhang, J. W. Cai, *APL Mater.* **2019**, 7, 041104.
- [22] L. Soumah, N. Beaulieu, L. Qassym, C. Carrétéro, E. Jacquet, R. Lebourgeois, J. Ben Youssef, P. Bortolotti, V. Cros, A. Anane, *Nat. Commun.* **2018**, 9, 3355.
- [23] Y. Zhang, Q. Du, C. Wang, W. Yan, L. Deng, J. Hu, C. A. Ross, L. Bi, *APL Mater.* **2019**, 7, 081119.
- [24] A. H. Eschenfelder, *Magnetic Bubble Technology*, Springer Berlin, Heidelberg **1980**.
- [25] S. A. Manuilov, S. I. Khartsev, A. M. Grishin, *J. Appl. Phys.* **2009**, 106, 123917.
- [26] L. Caretta, M. Mann, F. Büttner, K. Ueda, B. Pfau, C. M. Günther, P. Hensing, A. Churikova, C. Klose, M. Schneider, D. Engel, C. Marcus, D. Bono, K. Bagschik, S. Eisebitt, G. S. D. Beach, *Nat. Nanotechnol.* **2018**, 13, 1154.
- [27] S. A. Manuilov, A. M. Grishin, *J. Appl. Phys.* **2010**, 108, 13902.
- [28] S. A. Manuilov, R. Fors, S. I. Khartsev, A. M. Grishin, *J. Appl. Phys.* **2009**, 105, 033917.
- [29] B. Bhoi, B. Kim, Y. Kim, M. K. Kim, J. H. Lee, S. K. Kim, *J. Appl. Phys.* **2018**, 123, 203902.
- [30] J. C. Gallagher, A. S. Yang, J. T. Brangham, B. D. Esser, S. P. White, M. R. Page, K. Y. Meng, S. Yu, R. Adur, W. Ruane, S. R. Dunsiger, D. W. McComb, F. Yang, P. C. Hammel, *Appl. Phys. Lett.* **2016**, 109, 072401.
- [31] B. Bhoi, N. Venkataramani, S. Prasad, R. P. R. C. Aiyar, G. Kumar, I. Samajdar, M. Kostylev, *J. Magn. Magn. Mater.* **2019**, 483, 191.
- [32] R. Kumar, Z. Hossain, R. C. Budhani, *J. Appl. Phys.* **2017**, 121, 113901.
- [33] S. Estradé, J. M. Rebled, J. Arbiol, F. Peiró, I. C. Infante, G. Herranz, F. Sánchez, J. Fontcuberta, R. Córdoba, B. G. Mendis, A. L. Bleloch, *Appl. Phys. Lett.* **2009**, 95, 072507.
- [34] A. Bhattacharya, S. J. May, *Annu. Rev. Mater. Sci.* **2014**, 44, 65.
- [35] R. Bertacco, J. P. Contour, A. Barthélemy, J. Olivier, *Surf. Sci.* **2002**, 511, 366.
- [36] R. D. Shannon, *Acta Crystallogr. Sect. A: Found. Adv.* **1976**, 32, 751.
- [37] C. N. Wu, C. C. Tseng, Y. T. Fanchiang, C. K. Cheng, K. Y. Lin, S. L. Yeh, S. R. Yang, C. T. Wu, T. Liu, M. Wu, M. Hong, J. Kwo, *Sci. Rep.* **2018**, 8, 11087.
- [38] B. D. Cullity, C. D. Graham, *Introduction to Magnetic Materials*, John Wiley & Sons, Inc, Hoboken, NJ, USA **2008**.
- [39] E. A. Geiss, J. E. Davies, C. F. Guerci, H. L. Hu, *Mater. Res. Bull.* **1975**, 10, 355.
- [40] R. Wolfe, R. C. LeCraw, S. L. Blank, R. D. Pierce, *Appl. Phys. Lett.* **1976**, 815, 815.
- [41] T. Hibiya, H. Makino, S. Konishi, *J. Appl. Phys.* **1981**, 52, 7347.
- [42] N. Nakamura, H. Ogi, M. Hirao, T. Fukuhara, K. Shiroki, N. Imaizumi, *Jpn. J. Appl. Phys.* **2008**, 47, 3851.
- [43] H. T. Nembach, T. J. Silva, J. M. Shaw, M. L. Schneider, M. J. Carey, S. Maat, J. R. Childress, *Phys. Rev. B: Condens. Matter Mater. Phys.* **2011**, 84, 054424.
- [44] Y. Ding, T. J. Klemmer, T. M. Crawford, *J. Appl. Phys.* **2004**, 96, 2969.
- [45] I. Neudecker, G. Woltersdorf, B. Heinrich, T. Okuno, G. Gubbiotti, C. H. Back, *J. Magn. Magn. Mater.* **2006**, 307, 148.
- [46] S. S. Kalarickal, P. Krivosik, M. Wu, C. E. Patton, M. L. Schneider, P. Kabos, T. J. Silva, J. P. Nibarger, *J. Appl. Phys.* **2006**, 99, 093909.
- [47] R. O'Handley, *Modern Magnetic Materials: Principles and Applications*, Wiley, New York **1999**.
- [48] B. Heinrich, J. F. Cochran, R. Hasegawa, *J. Appl. Phys.* **1985**, 57, 3690.
- [49] C. Kittel, *Phys. Rev.* **1959**, 115, 1587.
- [50] M. C. Onbasli, A. Kehlberger, D. H. Kim, G. Jakob, M. Kläui, A. V. Chumak, B. Hillebrands, C. A. Ross, *APL Mater.* **2014**, 2, 106102.
- [51] T. B. Mitchell, P. E. Wigen, *J. Appl. Phys.* **1987**, 61, 3259.
- [52] S. Crossley, A. Quindeau, A. G. Swartz, E. R. Rosenberg, L. Beran, C. O. Avci, Y. Hikita, C. A. Ross, H. Y. Hwang, *Appl. Phys. Lett.* **2019**, 115, 172402.
- [53] P.-G. De Gennes, C. Kittel, A. M. Portis, *Phys. Rev.* **1959**, 116, 323.
- [54] M. H. Sirvetz, J. E. Zneimer, *J. Appl. Phys.* **1958**, 29, 431.
- [55] C. Kittel, *Phys. Rev.* **1946**, 70, 965.
- [56] A. Hubert, R. Schäfer, *Magnetic Domains: The Analysis of Magnetic Microstructures*, Springer, New York **1998**.
- [57] C. Kooy, U. Enz, *Philips Res. Rep.* **1960**, 15, 17.
- [58] F. Büttner, M. A. Mawass, J. Bauer, E. Rosenberg, L. Caretta, Can, O. A. , J. Gräfe, S. Finizio, C. A. F. Vaz, N. Novakovic, M. Weigand, K. Litzius, J. Förster, N. Träger, F. Groß, D. Suzuki, M. Huang, J. Bartell, F. Kronast, J. Raabe, G. Schütz, C. A. Ross, G. S. D. Beach, *Phys. Rev. Mater.* **2020**, 4, 011401.
- [59] B. Kaplan, G. A. Gehring, *J. Magn. Magn. Mater.* **1993**, 128, 111.
- [60] R. Schäfer, *J. Magn. Magn. Mater.* **2000**, 215, 652.